CRYSTAL GROWTH & DESIGN

pubs.acs.org/crystal

Article

Thermal-Driven Guest-Induced Spin Crossover Behavior in 3D Fe(II)-Based Porous Coordination Polymers

Published as part of a Crystal Growth and Design virtual special issue on Molecular Magnets and Switchable Magnetic Materials

Li Sun, Nour El Islam Belmouri, Mamadou Ndiaye, Koen Robeyns, Aurelian Rotaru, Kamel Boukheddaden, and Yann Garcia*

Cite This: *Cryst. Growth Des.* 2023, 23, 3402−3411

Read Online

ACCESS | Metrics & More | Article Recommendations | Supporting Information

ABSTRACT: 3D porous coordination polymers $[Fe(bpb)_2dca]$-ClO_4·0.5CH_3OH·Guest (bpb = 1,4-bis(4-pyridyl)benzene; Guest = chloroform or dichloromethane) (**1**·3$CHCl_3$ and **1**·2.5CH_2Cl_2, **1** = $[Fe(bpb)_2dca]ClO_4$·0.5CH_3OH) were synthesized and characterized by single-crystal X-ray diffraction, thermogravimetric, magnetic, optical, and calorimetric measurements. The 3D polymer **1**·3$CHCl_3$ displays upon cooling an incomplete one-step transition centered at $T_{1/2}$ ∼ 85 K according to SQUID measurements. The 3D polymer **1**·2.5CH_2Cl_2, however, displays a two-step incomplete spin crossover behavior located between $T_{1/2}$ ∼ 218 K for the highest transition and $T_{1/2}$ ∼ 124 K for the lower one. In addition, these materials show different colors due to accommodating chloroform (yellow color) or dichloromethane (orange color) molecules in their cavities. Cryogenic optical microscopy was used to image the spatiotemporal properties of the thermal transition at the scale of a single crystal of both compounds. A gradual transition with a homogeneous color change was detected in **1**·3$CHCl_3$ around 90 K, in fair agreement with magnetic data. In contrast, a cooperative hysteretic thermal transition accompanied by delamination and the appearance of well spatially organized microcracks was evidenced in **1**·2.5CH_2Cl_2 around 140 K. The complex two-step spatiotemporal front transformations observed in this system are attributed to the interplay between the SCO and the structural transition. In light of all the above elements, it is thus inferred that host−guest interactions in the crystal cavity can modulate these polymers' magnetic and optical properties. Such materials can realize the interconversion of high-spin and low-spin states under the stimulation of guest molecules, thus having potential applications as reusable storage for chemical and gas sensors.

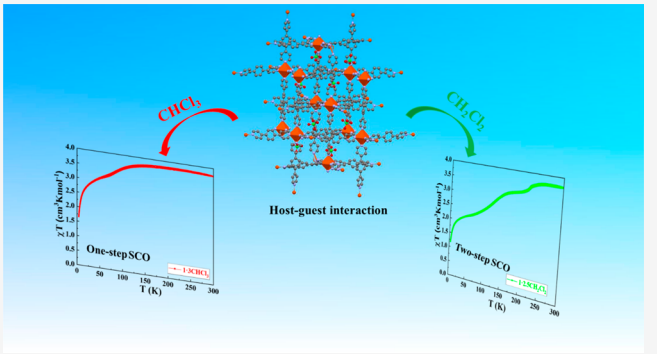

INTRODUCTION

Spin crossover (SCO) compounds can ideally display molecular bistability properties,[1,2] and the spin states of their Fe^{II} complexes ($3d^6$) can switch between a paramagnetic (S = 2) high-spin (HS) state and a diamagnetic (S = 0) low-spin (LS) state through external perturbations (e.g., temperature,[3] pressure,[4−6] magnetic field, light irradiation, analytes,[7] etc.).[8−10] The switch may be accompanied by changes in physical and chemical properties such as optical properties (color), magnetic behavior, and the presence of thermal hysteresis effects.[11,12] Thus, SCO compounds have potential practical applications in thermionic displays, optical switches, pressure sensors, and information storage.[13] Currently, the design and synthesis of new SCO compounds has become a growing research topic among coordination chemists.[14,15] In recent years, metal−organic frameworks (MOFs) or porous coordination polymers (PCPs) have become promising adsorbents for gas separation and purification due to their highly predictable and tunable properties in terms of pore size.[16,17] Therefore, 3D SCO-PCPs materials, with their dual functional characteristics of porosity and spin-state transformation, have become one of the most compelling research directions.[18,19] The porosity makes 3D porous SCO materials promising for gas or solvent molecule detection, with the adsorption/desorption of the guest molecule being able in turn to modulate the spin state of the material.[20,21]

Received: December 28, 2022
Revised: February 8, 2023
Published: March 31, 2023

Over the past decade, Real *et al.* made great contributions to the work on "molecular zeolite" materials with SCO properties.[22−31] Among them, the most representative 3D porous materials hold Hofmann-like structures, which usually display hysteretic SCO behavior.[32] For example, Real's group reported a series of 3D Hofmann-like clathrate porous SCO-PCP materials $[Fe^{II}(pz)M(CN)_4]\cdot nH_2O$[22] (pz = pyrazine; M = Ni^{II} (n = 2), Pd^{II} (n = 2.5), Pt^{II} (n = 2.5)), $\{Fe^{II}(pmd)(H_2O)[Ag(CN)_2]_2\}\cdot H_2O$[23] (pmd = pyrimidine), $\{Fe^{II}(azpy)[(M^{II}(CN)_4)]\}\cdot nH_2O$[33] (azpy = 4,4′-azopyridine; M = Ni^{II}, Pd^{II}, and Pt^{II}), $\{Fe^{II}(bpac)[Ag(CN)_2]_2\}$,[24] $[Fe^{II}(bpac)[M(CN)_4]$[25] (M = Pt^{II}, Pd^{II} and Ni^{II}; bpac = 4,4′-bis(pyridyl)-acetylene), $\{Fe^{II}(bpb)[Ag(CN)_2]_2\}$ and $\{Fe^{II}(bpb)[M(CN)_4]\}\cdot n$Guest[26] ($n$ = 2, Guest = naphthalene and nitrobenzene; M = Ni, Pd), $\{Fe^{II}(pina)[M(CN)_2]_2\}\cdot x$MeOH[28] ($x$ ∼ 5; pina = *N*-(pyridin-4-yl)isonicotinamide; M = Ag^I, Au^I), $\{Fe^{II}(bpan)[M(CN)_2]_2\}$ and $\{Fe^{II}(bpbd)[M(CN)_2]_2\}\cdot$pyrene (M = Ag^I, Au^I, bpan = bis(4-pyridyl)anthracene, bpbd = bis(4-pyridyl)butadiyne),[30] and $\{Fe^{II}(3,8phen)[Au(CN)_2]_2\}\cdot x PhNO_2$[20] (3,8phen = 3,8-phenanthroline, $PhNO_2$ = nitrobenzene). Most of the SCO complex systems with 3D porous PCP structures mentioned above can modulate the SCO behavior of the complexes using the adsorption/desorption of solvent molecules. In such cases, common interactions arising from the ability of the guest molecule to react with the host include van der Waals forces, hydrogen bonding, $\pi-\pi$ interactions, etc.[32] Recently, our group made a corresponding contribution to 3D clathrate porous SCO-PCP materials by discovering that chloroform molecules locked in the 3D Fe^{II} SCO-PCP complex $[Fe(bipy)_2dca]ClO_4\cdot CHCl_3\cdot CH_3OH$ (dca = $N(CN)_2^-$) based on 4,4′-bipyridine (bipy) were able to modulate the SCO behavior well, which was accompanied by a hysteresis loop of 15 K.[34] To better investigate the magnetic and optical properties of such 3D networks, on one hand, the length or flexibility of the building blocks can be appropriately increased to prepare SCO complexes with larger pores that can be used to lock a different amount or different sizes of solvent molecules in the crystal lattice and thus modulate the SCO behavior of these complexes. On the other hand, by changing the nature of the guest molecules, the interactions between the host and the guest can also be used to modulate the SCO behavior of the compound.

Here, we report the synthesis and characterization of two unprecedented 3D porous Fe^{II} SCO-PCPs complexes formulated as $[Fe^{II}(bpb)_2dca]ClO_4\cdot 0.5CH_3OH\cdot$Guest (**1**·Guest) (bpb = 1,4-bis(4-pyridyl)benzene in Scheme 1; dca = $N(CN)_2^-$; Guest = $3CHCl_3$, $2.5CH_2Cl_2$). Both clathrates undergo different SCO properties after locking $CHCl_3$ or CH_2Cl_2 in their crystal lattice. In addition, the SCO takes place in two steps for the CH_2Cl_2 clathrate (**1**·$2.5CH_2Cl_2$), while only a single step characterizes the SCO behavior for the $CHCl_3$ complex (**1**·$3CHCl_3$). Their molecular structures, physical characterization, and magnetic and optical properties are studied and revealed in detail. More importantly, magnetic characterization reveals the strong influence of the presence of $CHCl_3$ or CH_2Cl_2 guest molecules inside the pores of clathrates on the SCO properties, particularly revealing the generation of hysteretic spin transition, which may be associated with the presence of host−guest interactions.

Scheme 1. Molecular Structure of bpb

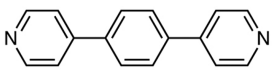

RESULTS AND DISCUSSION

Synthesis. Single crystals were grown by diffusing a solution of bpb in $CHCl_3$ or CH_2Cl_2 layered by a solution of $Fe(ClO_4)_2\cdot 6H_2O$, Nadca, and ascorbic acid in methanol at room temperature (298 K). NMR analysis indicates that methanol and chloroform (dichloromethane) molecules are locked in the crystal lattices of fresh crystals of **1**·$3CHCl_3$ (**1**·$2.5CH_2Cl_2$) (Figures S1 and S2). FT-IR spectra of such complexes are subtle, indicating similar functional groups (Figure S3). Further, the thermogravimetric analysis (TGA) curves recorded from room temperature up to 800 °C are shown in Figure 1. The first stage of weight loss (found/calcd. 28/35% for **1**·$3CHCl_3$ and 20/25% for **1**·$2.5CH_2Cl_2$) observed at around 200 °C indicates the loss of solvent molecules from the cavities of the structure, and the next stages are presumably associated with the collapse of the material framework and the decomposition of the ligands. These materials thus show thermal stability up to 200 °C. The compounds $[Fe(bpb)_2dca]ClO_4\cdot 2H_2O\cdot 1.5CHCl_3$ (**2**) and $[Fe(bpb)_2dca]ClO_4\cdot 2H_2O\cdot CH_2Cl_2$ (**3**) were obtained by partial desolvation of **1**·$3CHCl_3$ and **1**·$2.5CH_2Cl_2$ at 120 °C for 40 min, respectively (Figure S4), as a consequence of the replacement of $CHCl_3$ or CH_2Cl_2 and methanol molecules by H_2O from atmospheric humidity. The number of solvent molecules in the molecular formula (**1**·$3CHCl_3$, **1**·$2.5CH_2Cl_2$, **2**, and **3**) were determined by thermogravimetric and elemental analyses. The framework complexes (**1**·$3CHCl_3$ and **1**·$2.5CH_2Cl_2$) were determined by single crystal X-ray diffraction. For compounds **2** and **3**, given that after partial desolvation, the crystal quality was no longer suitable for single crystal X-ray diffraction analysis.

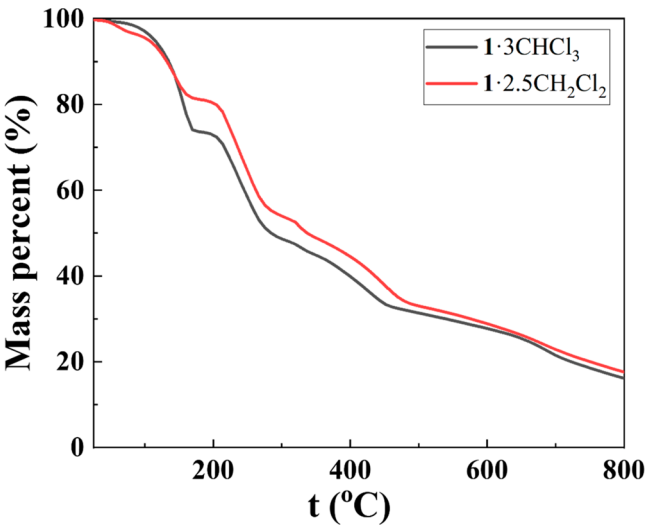

Figure 1. TGA curves of **1**·$3CHCl_3$ and **1**·$2.5CH_2Cl_2$.

Complex **1** depends on solvent molecules to induce and adjust its SCO properties (see Figure 6), and the inclusion of different solvent molecules in the lattice will result in crystals with different colors, such as yellow (orange) when $CHCl_3$ (CH_2Cl_2) is in the lattice of SCO PCP **1** at room temperature (Figure 2). Additionally, at 77 K, a thermochromic effect is observed with yellow crystals of **1**·$3CHCl_3$ turning to dark

https://doi.org/10.1021/acs.cgd.2c01538
Cryst. Growth Des. 2023, 23, 3402−3411

brown, whereas orange crystals of $1{\cdot}2.5CH_2Cl_2$ change to almost black.

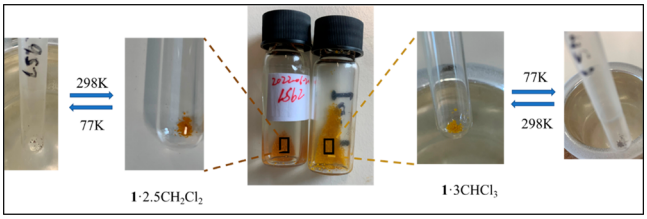

Figure 2. Color changes of $1{\cdot}3CHCl_3$ and $1{\cdot}2.5CH_2Cl_2$ between 298 and 77 K.

Single-Crystal X-ray Structures. To investigate the guest dependence of the SCO behavior, single-crystal data were collected for $1{\cdot}3CHCl_3$ at 100 and 297 K (Figure 3 and Table 1). At 100 K, the structure exhibited the monoclinic $P2/c$ space group. The equatorial positions of the octahedra are coordinated by four ligands, which build up 2D infinite $[Fe(bpb)_2]_\infty^{2+}$ sheets. The apical positions are occupied by $N(CN)_2^-$ groups acting as connections between adjacent sheets, thereby defining a 3D framework (Figure 3). The average Fe−N bond length, 2.180 Å, which indicates that the Fe^{II} ions are in the HS state at 100 K, a fact consistent with magnetic data (see Figure 7). Each network is interpenetrated by another identical net, a two-layer penetrated topology, leaving void space within the structure. There are intermolecular contacts in the structure of $1{\cdot}3CHCl_3$ at 100 K that are shorter than the van der Waals bond length, including chloroform···ligand bpb, and chloroform···perchlorate ions (Figure S5). Single-crystal X-ray diffraction data collected at 297 K showed limited diffraction, which is presumably due to the loss of solvent molecules leading to a decrease in crystal quality. The unit cell is unchanged upon heating to 297 K, apart from the expected thermal expansion, showing the same symmetry (Table 1).

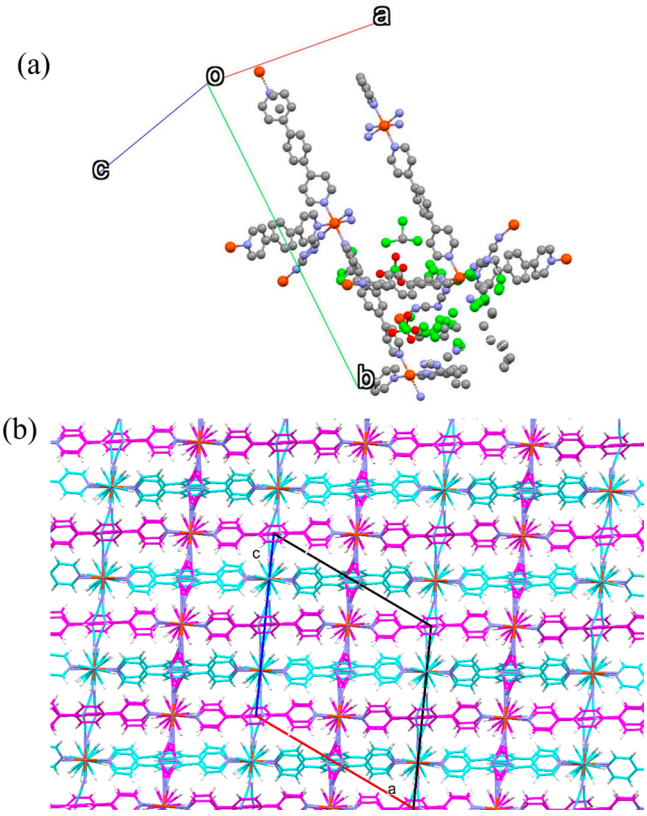

Figure 3. (a) Unit cell of $1{\cdot}3CHCl_3$ at 100 K, where Fe (orange), O (red), N (blue), C (gray), and Cl (green). (b) View along the *b*-axis. Anions, solvent molecules, and disordered parts were omitted for clarity.

Single crystal data of $1{\cdot}2.5CH_2Cl_2$ were collected at 297, 185, and 120 K (Figures 4 and 5 and Table 1). At 297 K, the structure of $1{\cdot}2.5CH_2Cl_2$ shows the orthorhombic $I222$ space group. At 120 and 185 K, the space group changes, however, to the monoclinic $I2$ space group. Both structures are basically identical, and at room temperature the disorder observed at low temperature is averaged out, leading to a higher-symmetry structure. Fe^{II} ions are coordinated by six N atoms, FeN_6, and the equatorial coordination sites of Fe^{II} are occupied by four bpb molecules, while its axial positions are occupied by two $[N(CN)_2]^-$ units. The $[N(CN)_2]^-$ groups are linear to connect 2D infinite $[Fe(bpb)_2]_\infty^{2-}$ sheets to form a 3D framework (Figure 4 and 5). Each network is interpenetrated by another identical one. The Fe···Fe distance connected by $[N(CN)_2]^-$ is 8.635 Å (8.471 Å,120 K; 8.530 Å, 185 K) and that connected by bpb ligands is 15.80 Å (15.667 Å, 120 K; 15.734 Å, 185 K) at 297 K. The average Fe−N bond length is 2.194 Å in the HS state at 297 K. However, in the crystal structure taken at 120 K, the average Fe−N bond length, 2.042 Å, indicates that the Fe atoms are in a mixed HS/LS state, a result consistent with magnetic susceptibility data (Figure 6). At 120 K, it is apparent that van der Waals interactions exist between CH_2Cl_2 molecules and bpb ligands (Figure S6). When they were cooled in liquid N_2, crystals of $1{\cdot}2.5CH_2Cl_2$ showed dramatic color changes from orange to almost black (Figure 2), indicating the occurrence of a HS to LS transition of the Fe^{II} ions (the thermochromic effect is reversible, with the black crystals turning orange again they are removed from liquid N_2, showing a LS to HS SCO of the central Fe^{II} ions).

2.3. Magnetic Properties. The temperature dependence of χT was also produced for different phases of compounds **1**·Guest by cooling and heating to study the effect of guest molecules on the SCO properties (Figure 6). For all compounds, the values of χT are around 3.8 $cm^3\ mol^{-1}\ K$ at room temperature, which indicated that all Fe^{II} centers are in the HS state ($S = 2$). $1{\cdot}3CHCl_3$ and $1{\cdot}2.5CH_2Cl_2$ exhibit a gradual and incomplete SCO behavior. For $1{\cdot}3CHCl_3$, $T_{1/2} \sim 85$ K as the temperature decreases, and there is no hysteresis (Figure S8). When the temperature is reduced to 45 K, a HS distribution of 87% is still maintained. However, for **1**·$2.5CH_2Cl_2$, an incomplete two-step SCO behavior is observed, involving ~7% of Fe^{II} ions in the first step from 250 to 180 K with $T_{1/2} \sim 218$ K and ~41% of Fe^{II} ions from 180 to 33 K with $T_{1/2} \sim 124$ K (Figure S7). Thus, magnetic property data indicate that solvent molecules ($CHCl_3$ or CH_2Cl_2) can induce different SCO behaviors. In addition, these materials show a color change from orange (yellow) to almost black (dark brown) upon cooling from 298 to 77 K. When solvent molecules partly escape from the crystal lattice upon warming at 120 °C for 40 min, the SCO behaviors of the resulting compounds (**2** and **3**) are canceled (Figure S9). Indeed, central Fe^{II} ions are almost no longer sensitive to temperature change and show a HS state over the whole temperature range. To further study the effect of solvent molecules on the SCO behavior of complexes, we shall take $1{\cdot}2.5CH_2Cl_2$ as a

https://doi.org/10.1021/acs.cgd.2c01538
Cryst. Growth Des. 2023, 23, 3402−3411

Table 1. Crystal Data and Structure Refinement Details for As-Synthesized Complexes 1·Guest at 120, 185, and 298 K

identification code	1·3CHCl$_3$	1·3CHCl$_3$	1·2.5CH$_2$Cl$_2$	1·2.5CH$_2$Cl$_2$	1·2.5CH$_2$Cl$_2$
empirical formula	4($C_{34}H_{24}FeN_7$), 4(ClO_4), 11($CHCl_3$) [+ solvent]	$C_{34}H_{24}FeN_7$, ClO_4, 0.693($CHCl_3$) [+ solvent]	$C_{68}H_{48}Fe_2N_{14}$, 2(ClO_4), 3.394(CH_2Cl_2) [+ solvent]	$C_{70.12}H_{52.24}Cl_{6.24}Fe_2N_{14}O_8$	$C_{34}H_{24}FeN_7$, ClO_4 [+ solvent]
formula weight	4056.65	768.69	1660.09	1551.74	685.90
T (K)	100(2)	297(2)	120(2)	185(2)	297(2)
wavelength (Å)	0.71073	0.71073	0.71073	0.71073	0.71073
crystal system	monoclinic	monoclinic	monoclinic	monoclinic	orthorhombic
space group	$P2/c$	$P2/c$	$I2$	$I2$	$I222$
unit cell dimensions (Å,°)	a = 17.2660(8)	a = 17.567(2)	a = 16.9076(4)	a = 17.0603(6)	a = 17.2692(5)
	b = 31.6010(14)	b = 31.598(4)	b = 31.2943(7)	b = 31.4671(10)	b = 31.5997(9)
	c = 17.3090(9)	c = 17.475(3)	c = 31.2889(7)	c = 31.4888(11)	c = 31.6323(9)
	α = 90	α = 90	α = 90	α= 90	α = 90
	β = 114.880(6)	β = 116.368(18)	β = 90.051(2)	β= 90.109(3)	β= 90
	γ = 90	γ = 90	γ = 90	γ = 90	γ = 90
V (Å^3)	8567.7(8)	8691(2)	16555.3(7)	16904.3(10)	17261.8(9)
Z	2	8	8	8	16
density (calc.) (g cm^{-3})	1.572	1.175	1.332	1.219	1.056
absorption coefficient (mm^{-1})	0.977	0.576	0.693	0.595	0.449
F(000)	4092	3138	6773	6344	5632
crystal size (mm^3)	0.100 × 0.040 × 0.030	0.25 × 0.18 × 0.15	0.22 × 0.20 × 0.10	0.43 × 0.33 × 0.08	0.20 × 0.12 × 0.07
θ-range for data collection (°)	2.282 to 25.316	2.888 to 22.131	2.911 to 26.048	2.893 to 25.252	2.263 to 25.264
reflections collected	78419	10366	27684	28985	15365
independent reflections	15302 [$R_{(int)}$ = 0.0950]	10366 [R(int) = 0][a]	27684 [$R_{(int)}$ = 0][a]	28985 [R(int) = 0][a]	15365 [$R_{(int)}$ = 0][a]
completeness to (%)	98.2 (θ = 25.242°)	95.3 (θ = 22.131°)	98.6 (θ = 25.242°)	96.5	99.5 (θ = 25.242°)
max. and min. transmission	0.971 and 0.660	1.00000 and 0.91797	1.00000 and 0.85473	1.00000 and 0.76122	1.00000 and 0.84496
refinement method	full-matrix least-squares on F^2				
data/restraints/parameters	15302/605/1287	10366/1130/953	27684/2441/1975	28985/2298/1904	15365/1502/1091
goodness-of-fit on F_2	1.091	1.057	1.228	1.480	1.099
final R indices (I > 2s(I))	R_1 = 0.0943, wR_2 = 0.2077	R_1 = 0.1625, wR_2 = 0.3498	R_1 = 0.0796, wR_2 = 0.1915	R_1 = 0.1125, wR_2 = 0.2668	R_1 = 0.0714, wR_2 = 0.1636
R indices (all data)	R_1 = 0.1355, wR_2 = 0.2297	R_1 = 0.2287, wR_2 = 0.3968	R_1 = 0.0858, wR_2 = 0.1978	R_1 = 0.1218, wR_2 = 0.2727	R_1 = 0.1176, wR_2 = 0.1943
abs. struct. parameter			0.029(13)	0.067(11)	0.02(2)
$\Delta\rho$ (max, min) (e Å^{-3})	1.357, −0.808	1.560, −0.951	1.199, −0.921	1.120, −1.383	0.686, −0.528

[a]Twin refinement (HFLF 5 formatted data, merge 0).

representative example (Figure S10). First of all, the magnetic properties of this material were recorded upon cooling from 300 to 4 K and then upon warming back to 300 K as a first run, showing the expected two-step SCO behavior presented in Figure 6. After that, the sample was cooled to 4 K and warmed back again, but this time to 400 K for annealing during 30 min as the second run. The χT values are similar in the first two cycles from 4 to 300 K, although a small deviation is observed below 150 K (Figure S10). After annealing at 400 K, the χT profile for the third run upon cooling and warming back to 400 K (Figure S10) shows a paramagnetic-like behavior involving a few spins.[35] Nevertheless, the χT values are maintained at 3.5−3.8 cm^3 mol^{-1} K, whatever the run, which indicates that almost all Fe^{II} ions remain in the HS state after the solvent molecules are partially removed from the cavities of the compound. Therefore, the behavior of the vanishing SCO behavior might be attributed to the deterioration of host−guest interactions and the deformation of the framework during desolvation.

2.4. Differential Scanning Calorimetry (DSC). DSC measurements were also performed for 1·2.5CH$_2$Cl$_2$ (Figure 7) over the temperature range 115−300 K upon cooling and heating at a scan rate of 2 K min^{-1}. In heating mode, the heat capacity profile, C_p, reveals an endothermic peak, characteristic of a first order phase transition, observed at an onset temperature $T_0^{\uparrow}$ = 220 K (ΔH = 4.1 kJ mol^{-1} and ΔS = 17.7 J mol^{-1} K^{-1}). In the cooling mode, an exothermic peak is

https://doi.org/10.1021/acs.cgd.2c01538
Cryst. Growth Des. 2023, 23, 3402−3411

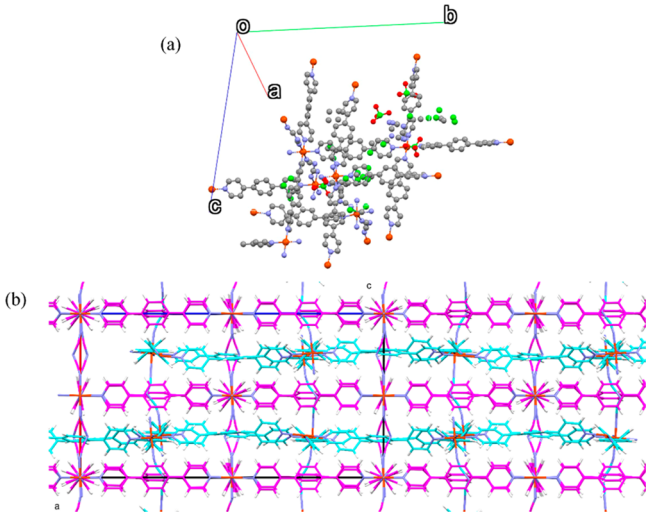

Figure 4. (a) Unit cell of **1**·2.5CH_2Cl_2 at 120 K, where Fe (orange), O (red), N (blue), C (gray), and Cl (green). (b) View along the *b*-axis. Anions, solvent molecules, and disordered parts were omitted for clarity.

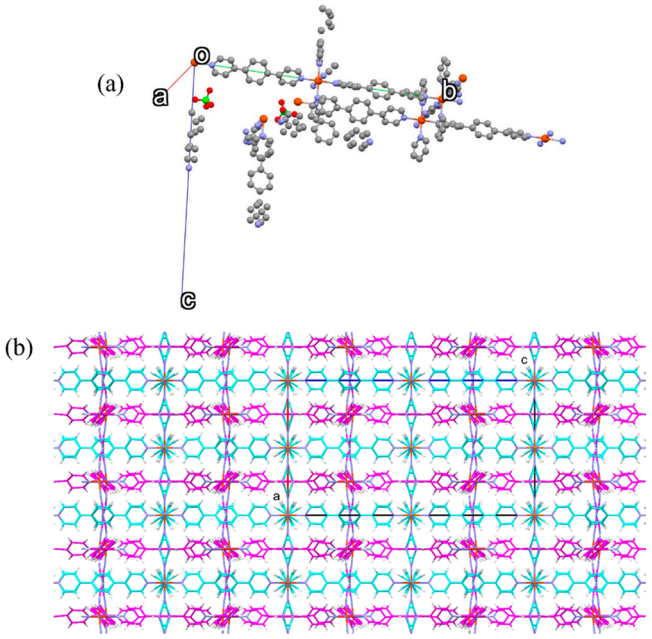

Figure 5. (a) Unit cell of **1**·2.5CH_2Cl_2 at 297 K, where Fe (orange), O (red), N (blue), C (gray), and Cl (green). (b) View along the *b*-axis. Anions, solvent molecules, and disordered parts were omitted for clarity.

observed at a similar temperature, showing no hysteresis effect. Such a phase transition actually corresponds well to the high-temperature branch of the SCO curve delineated by the magnetic data ($T_{1/2}^{\uparrow}$ = 219 K, $T_{1/2}^{\downarrow}$ = 217 K), thus showing almost no hysteresis (Figure 6). No DSC signal could be recorded for the low-temperature branch. The same applies for **1**·3$CHCl_3$.

2.5. Optical Microscopy. Cryogenic optical microscopy (OM) studies on a single crystal of **1**·3$CHCl_3$ were performed at variable temperatures in order to investigate the spatiotemporal properties associated with its SCO behaviors. The quantitative analysis of the OM data was performed by tracking the evolution of the transmitted light intensities of the

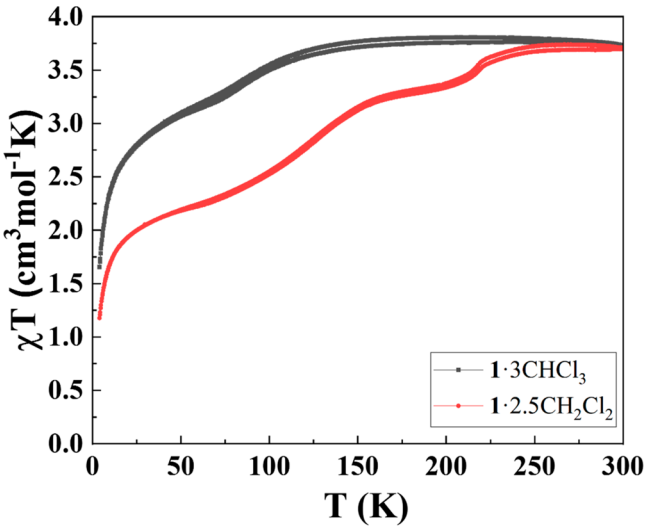

Figure 6. Plots of χT vs T for **1**·3$CHCl_3$ and **1**·2.5CH_2Cl_2.

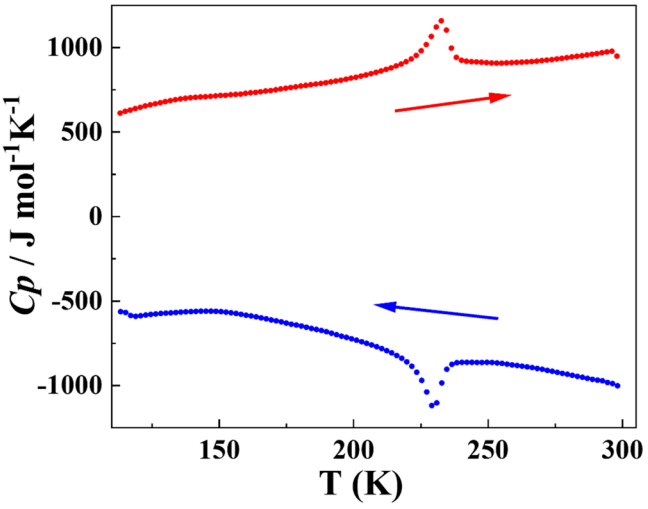

Figure 7. Heat capacity thermal profile of the cooling and warming of **1**·2.5CH_2Cl_2 recorded at a scan rate of 2 K min^{-1}.

RGB (red, green, and blue) pixels from which the local and averaged optical densities were derived, which directly connect to the HS fraction of the material.[36,37] The results of the thermal dependence of the HS fraction of **1**·3$CHCl_3$, derived from OM are summarized in Figure 8, where the SCO is found to proceed gradually over the range 60−200 K without any noticeable hysteresis. A good match is observed with the magnetic susceptibility measurements of Figure 6. OM data were analyzed using an Ising model (see the Experimental Section). A fair agreement is found in the following ranges of numerical parameters: Δ = 278.4 K, J = 140 K, and $g \sim 18.17$, leading to the respective molar enthalpy and entropy changes $\Delta H \sim 2.3$ kJ mol^{-1} and $\Delta S \sim 24.1$ J K^{-1} mol^{-1}, (with $T_{1/2}$ = 96 K) (Figure 8). The present theoretical analysis also shows that the interaction parameter J is quite small compared to the ligand field energy Δ due to the very gradual character of the transition, which was derived from OM observations.

The video of **1**·3$CHCl_3$ (Movie S1) shows the occurrence of a gradual transition without front detection. Some stripes at the crystal surface are visible (Figure 8b).

Cryogenic OM studies of a selected single crystal of **1**·2.5CH_2Cl_2, were performed over the range 70−270 K. The

https://doi.org/10.1021/acs.cgd.2c01538
Cryst. Growth Des. 2023, 23, 3402−3411

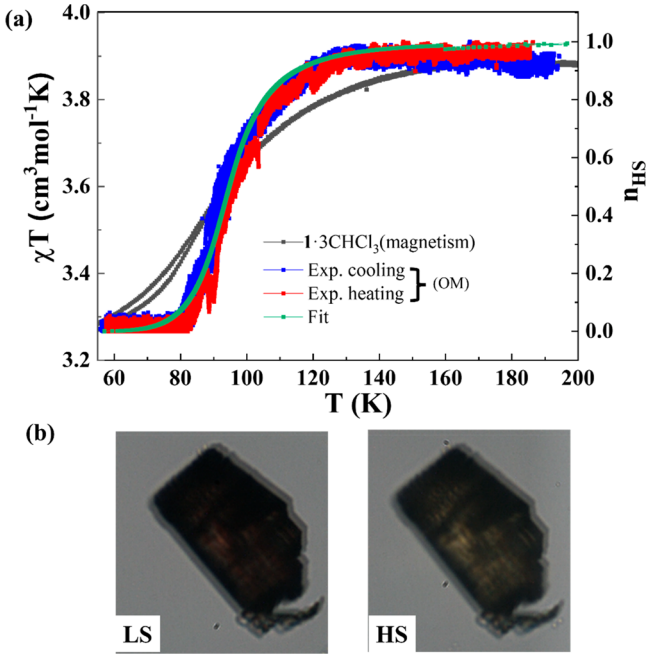

Figure 8. (a) Thermal dependence of the averaged HS fraction deduced from optical density for a crystal of **1**·3$CHCl_3$ in both cooling (in blue) and warming (in red) modes, at 0.5 K min^{-1}. The fit (olive color) derived from an Ising-like model is also shown along with the magnetic measurements (black) after a first run for comparison (derived from Figure 6). (b) Selected crystal images showing the spatiotemporal behavior of transmission images at characteristic temperatures 200 and 60 K in both HS and LS states, respectively.

typical crystal sizes are ∼75.6 μm length and ∼74.2 μm width. Initially the crystal quality is quite good and the sample is colored. Two transitions are revealed: a first one that is gradual between 280 and 150 K and a second one more abrupt and hysteretic in nature centered around 145 K (Figure 9a). Given the hysteretic nature of the second transition, it was analyzed using an Ising model (see the Experimental Section). As shown in Figure 9b, a fair agreement is found in the following ranges of numerical parameters: $\Delta \approx 493.14$ K, $J = 340$ K and g∼28.80, leading to the respective molar enthalpy and entropy changes ΔH∼4.10 $kJmol^{-1}$ and ΔS∼27.93 $JK^{-1}mol^{-1}$, (with $T_{1/2} = 147$ K). Such hysteresis loop was not observed clearly during magnetic measurements, which involve a large number of microcrystals.

Analysis of the movie associated to the cooling of **1**·2.5CH_2Cl_2 (Movie S2) shows the existence of two transitions. The first one starts at the beginning of the experiment (270 K) around the center of the crystal whose color changes gradually down to 150 K, followed by a second transition that is much faster and accompanied with a front interface evolving toward the edges of the crystal by generating dislocations (fractures and defects) that have two preferential directions (with angles equal to 45° and − 45°). Lastly, a third transition that is assimilated with a hysteresis effect starts at 144 K from the dislocations with significant color change, evolving in all directions as seen in Figure 10a and b. In the heating mode, a front starting from the edges and going toward the center of the crystal is observed around 150 K. Next, dislocations start to disappear, and finally the center changes its color gradually, where that of HS is recovered at 270 K. Interestingly, the fractures (delamination and microcracks) that were present in

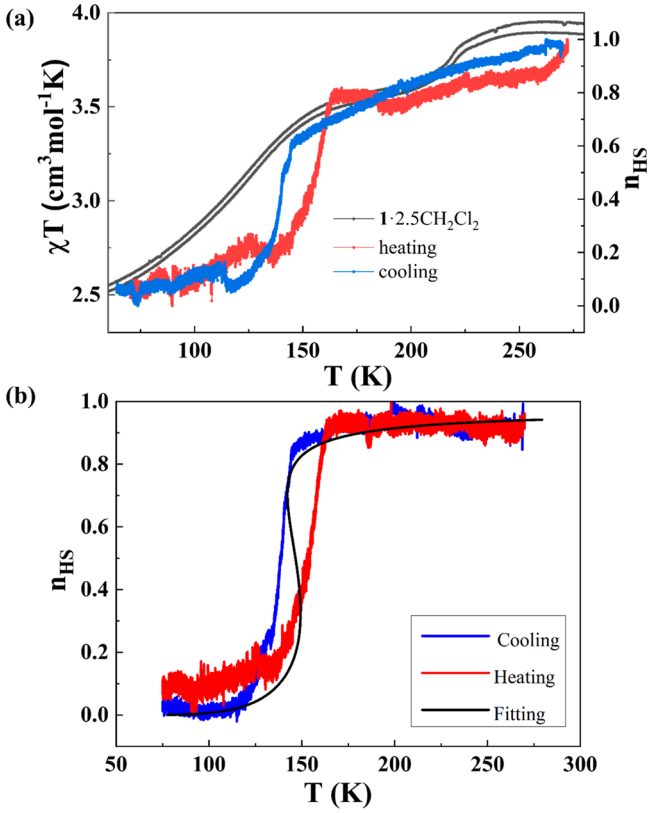

Figure 9. (a) Thermal dependence of the averaged HS fraction (deduced from optical density) for a crystal of **1**·2.5CH_2Cl_2 (first run of **1**·2.5CH_2Cl_2) in both cooling (blue) and warming (red) modes at 2 K min^{-1} along with the magnetic data (gray brown). (b) The best fitting (black line) derived from the Ising-like model for the hysteretic part after data normalization.

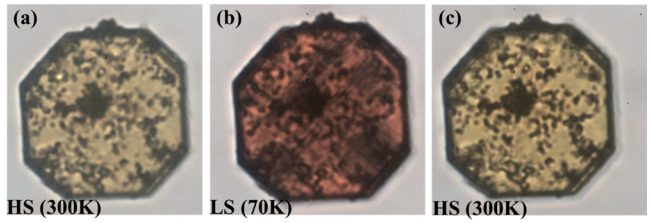

Figure 10. Images of the crystal **1**·2.5CH_2Cl_2 (a) at 300 K (HS state) at the beginning of the experiment, (b) at 70 K (LS state) after cooling, and (c) at 300 K (HS) after one thermal cycle.

the LS state disappear in the HS phase, as shown in Figure 10c, evidencing a self-reparation process.

According to the previous discussion, it is concluded that the center and the border of the crystal have different behaviors and do not react simultaneously to the transition. The transition of the center is gradual and starts almost from the beginning of the experiment, with a regime change at 145 K. Above 145 K, the edge is insensitive to the phase change; below 145 K, the transition at the edges takes place, and it is more abrupt than that of the center. This point will also be discussed in the next paragraphs.

A second experiment was carried out on the same crystal of **1**·2.5CH_2Cl_2, but the previous light front that triggered the appearance of dislocations/fractures along the cooling mode was no longer observed, while the dislocations still existed and

https://doi.org/10.1021/acs.cgd.2c01538
Cryst. Growth Des. 2023, 23, 3402−3411

appeared more abruptly. The corresponding data are summarized in Figure 11.

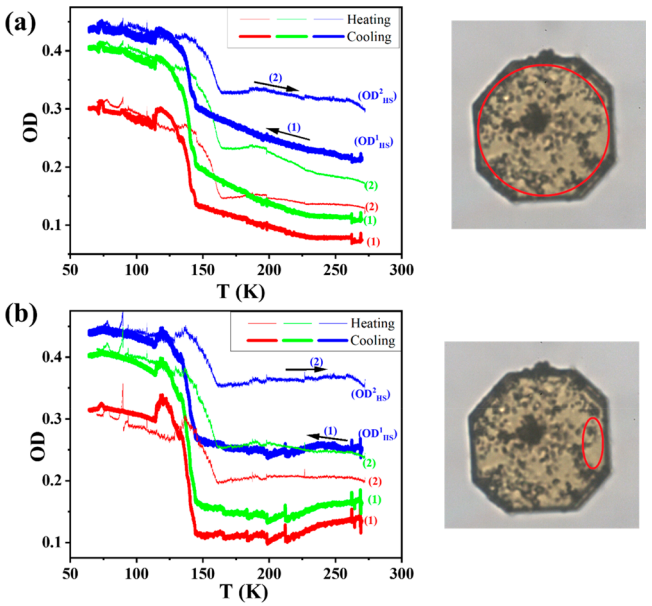

Figure 11. Optical density vs T for a crystal of **1**·2.5CH_2Cl_2 measured (a) on the whole crystal (see the corresponding image) and (b) around the edge in the region surrounded by the red circle (see the corresponding image).

Inspection of Figure 11 show that the value of the OD of the LS state appears to be reversible for the heating and cooling processes. In contrast, that of the HS is significantly affected by the thermal history. Indeed, the experiments have been performed by starting first from the HS state by cooling the sample from 270 K, where the OD_1^{HS} of the blue channel has level (1). On warming, we do reach the HS state with another value, OD_2^{HS} of the blue pixel, that is level (2) (Figure 11). We observe the same effect on the other channels, where the levels of OD_1^{HS} of the HS state of the red and green channels are lower than OD_2^{HS}, as shown in Figure 11, with the levels (1) and (2) corresponding to each channel.

Thus, upon cooling, the crystal reaches the $OD_1^{LS} > OD_1^{HS}$ signal of the LS state with the appearance of well-oriented dislocations and microcracks, which strongly alter the crystal's microstructures as well as its integrity. As a result, upon heating from this state, although we still observe the SCO transition, the level of OD of the HS state is significantly affected by the presence of these cracks and defects, which causes light scattering. This leads to a decrease in the intensity of transmitted light through the crystal, resulting in an increase of the OD. It is worth noticing that the difference ($\Delta OD_{HS} = OD_2^{HS} - OD_1^{HS}$) strongly depends on the considered channel (RGB) and seems to decrease for the red channel as compared with the green and the blue ones.

Another interesting observation confirming the difference of responses of the center and edge of the crystal is easily visible in Figure 11a and b, which present the OM data of the whole crystal and the edge, respectively. In the cooling mode, all curves of the three channels of Figure 11a (whole crystal) show a gradual increase of the OD in the temperature range 270−145 K, while those of Figure 11b (the edge) evidence a more or less constant OD in the same temperature range.

CONCLUSION

In this work, we have reported two 3D clathrates, [Fe(bpb)$_2$dca]ClO_4·0.5CH_3OH·Guest (Guest = $CHCl_3$ or CH_2Cl_2) and shown that their magnetic and optical properties can be modulated by guest solvent molecules. The spin crossover behavior takes place in two steps for the CH_2Cl_2 clathrate (HS, orange; LS, almost black), while only a one step characterizes the SCO behavior for the $CHCl_3$ complex (HS, yellow; LS, dark brown). In addition, the spin crossover behaviors of partial desolvation **2** (**3**) are silenced, a phenomenon accompanied by a color change from yellow (orange) to dark brown. Optical microscopy measurements performed at variable temperatures on unique single crystals for both compounds confirmed the magnetic and calorimetric measurements. Indeed, no front transformation was detected in the $CHCl_3$ complex, which experiences continuous and reversible changes between the LS and the HS phases with a global color change of the crystal, in agreement with the absence of hysteretic transition observed in magnetism. On the other hand, CH_2Cl_2 showed a violent hysteretic thermal transition with front interfaces, combining intricate and complex structural and electronic changes, which were revealed through the successive change of color and appearance of cracks in the crystal. Therefore, combined with single crystal diffraction analysis, the study speculates that tuning spin crossover behavior in this family of materials may be provided by a series of intramolecular and intermolecular interactions. Finally, the present study demonstrates an interesting multichannel controllable color and spin states change at different temperatures, and these 3D frameworks are potentially exciting materials for constructing sensor devices.

EXPERIMENTAL SECTION AND THEORETICAL MODELING

Materials and Characterization Methods. $Fe(ClO_4)_2·6H_2O$ (Acros organic), sodium dicyanamide (Nadca) (Fluorochem), and 1,4-bis(4-pyridyl)benzene (bpb) (Zhengzhou Alfa Chemical Co., Ltd.) were purchased and used as received without further purification. Elemental analyses for C, H, and N were performed by Medac Ltd. (UK). Fourier transformed infrared (FT-IR) spectroscopy measurements were performed using an Equinox 55 (Bruker) system equipped with an ATR modulus and an MCT detector. The Bruker software OPUS was used for data treatment (including ATR correction). Thermogravimetric analyses (TGA) were performed in a $N_{2(g)}$ atmosphere at a heating rate of 5 °C min^{-1} from 25 to 850 °C using a Mettler Toledo TGA/SDTA 851e analyzer. DSC measurements were performed on a Mettler Toledo DSC analyzer in a $N_{2(g)}$ atmosphere at a heating rate of 2 K min^{-1} from 115 to 298 K. Magnetic susceptibilities were measured on a quantum design MPMS-5s SQUID magnetometer at 1000 G and a scan rate of 2 K min^{-1}. Magnetic data were corrected for the sample holder and diamagnetic contributions. The crystal sample was quickly loaded into a gelatin capsule and immediately inserted into the SQUID cavity.

Syntheses. [Fe(bpb)$_2$dca]ClO_4·0.5CH_3OH·3$CHCl_3$ (**1**·3$CHCl_3$): bpb (4.6 mg, 0.02 mmol) was dissolved in chloroform (1 mL) (at the bottom of a 4 mL tube) and layered below a filtered Fe^{II}/dca solution formed in an ascorbic acid solvent environment (to prevent Fe^{II} oxidation) from $Fe(ClO_4)_2·6H_2O$ (7.3 mg, 0.02 mmol) and Nadca (1.8 mg, 0.02 mmol) in methanol (1 mL). A layer of a buffer solvent (containing V_{CHCl_3}/V_{MeOH} = 1:1, 1 mL) was placed between both layers to prevent instant precipitation of a powder. After a few days, yellow crystals were formed at the interface of the layers. Yield ∼62% (6.6 mg). Elemental analysis (%) for $FeC_{37.5}H_{29}N_7Cl_{10}O_{4.5}$. Calcd.: C 42.52, H 2.55, N 9.26. Found: C 43.03, H 2.51, N 9.60. IR (cm^{-1}): 532, 547, 579, 620, 666, 719, 746, 811, 836, 864, 1008, and 1084.

https://doi.org/10.1021/acs.cgd.2c01538
Cryst. Growth Des. 2023, 23, 3402−3411

$[Fe(bpb)_2dca]ClO_4{\cdot}0.5CH_3OH{\cdot}2.5CH_2Cl_2$ (**1**·2.5CH_2Cl_2): orange crystals of **1**·2.5CH_2Cl_2H were prepared in a similar method to that of **1**·3$CHCl_3$ using CH_2Cl_2. Yield ∼79% (7.2 mg). Elemental analysis (%) for $FeC_{37}H_{31}N_7Cl_6O_{4.5}$. Calcd.: C 48.66, H 3.40, N 10.74. Found: C 48.17, H 3.18, N11.02. IR (cm^{-1}): 532, 547,579, 620, 719, 733, 809, 835, 864, 1009, and 1085.

The compounds $[Fe(bpb)_2dca]ClO_4{\cdot}2H_2O{\cdot}1.5CHCl_3$ (**2**) and $[Fe(bpb)_2dca]ClO_4{\cdot}2H_2O{\cdot}CH_2Cl_2$ (**3**) were obtained by partial desolvation of **1**·3$CHCl_3$ and **1**·2.5CH_2Cl_2 at 120 °C for 40 min, respectively. $[Fe(bpb)_2dca]ClO_4{\cdot}2H_2O{\cdot}1.5CHCl_3$ (**2**): Elemental analysis (%) for $FeC_{35.5}H_{29.5}N_7Cl_{5.5}O_6$. Calcd.: C 47.32, H 3.30, N 10.88. Found: C 47.70, H 3.11, N 10.78. $[Fe(bpb)_2dca]ClO_4{\cdot}2H_2O{\cdot}CH_2Cl_2$ (**3**): Elemental analysis (%) for $FeC_{35}H_{30}N_7Cl_3O_6$. Calcd.: C 52.10, H 3.75, N 12.15. Found: C 51.40, H 3.47, N 12.02.).

Optical Microscopy. Optical microscopy measurements were carried out under a primary vacuum on single crystals (length × width = 111.13 μm × 59.11 μm for **1**·3$CHCl_3$ and 75.66 μm × 74.22 μm for **1**·2.5CH_2Cl_2) using a Nikon Eclipse LV100 microscope (objective ×20, numerical aperture 0.4), equipped with a closed cycle Oxford Instruments nitrogen-flow cryostat and connected to a digital camera Coreview Dalsa Falcon 1:4 M100 HG color camera capable of capturing up to 100 frames per second. The OM images were recorded in transmission geometry using backward illumination by a tungsten halogen lamp, which was provided by the microscope. The sample was mounted in specific helium-tight cell designed for optical microscopy.[38] All measurements were performed using a temperature scan rate of 0.5 K min^{-1} for **1**·3$CHCl_3$ and 2 K min^{-1} for **1**·2.5CH_2Cl_2. The camera was configured to save 100 images per second to record the spatiotemporal behavior of the spin transition. From every saved image, we can extract the optical density (OD), which is defined as

$$\mathrm{OD} = \log_{10}\left(\frac{I_{\mathrm{incident}}}{I_{\mathrm{transmitted}}}\right) \tag{1}$$

where I_{incident} corresponds to the bright-field intensity and $I_{\mathrm{transmitted}}$ corresponds to the intensity of the transmitted light through the single crystal. The OD, which is the key parameter of the OM data analysis (recorded images), directly relates to the HS fraction, n_{HS}, of the single crystal, corresponding to the fraction of metal ions in the HS state, through the relation[39]

$$n_{\mathrm{HS}} = \frac{\langle \mathrm{OD}(x,y)\rangle - \mathrm{OD}_{\mathrm{LS}}}{\mathrm{OD}_{\mathrm{HS}} - \mathrm{OD}_{\mathrm{LS}}} \tag{2}$$

where $\mathrm{OD}_{\mathrm{HS}}$ and $\mathrm{OD}_{\mathrm{LS}}$ are respectively the OD values in the HS and LS states and $\langle \mathrm{OD}(x,y)\rangle$ is the spatially averaged optical density over the crystal at given temperature, T. In addition, each image of the experimental OM data was split into three OD components: red, green, and blue, whose responses depend on the single crystal thickness, color, and microstructure. From one compound to another, the signal quality (signal-to-noise ratio) would perhaps be better in either the red, green, or blue pixel. All the data are analyzed using Matlab programs developed by the Versailles group.

Modeling. The Ising model is used here to describe the SCO from the HS to the LS state by representing these states with fictitious spin states +1 and −1, respectively. The expression of the Hamiltonian of the system is given by[40]

$$H = -J\sum_{i,j} S_iS_j + \sum_i \Delta_{\mathrm{eff}}S_i \tag{3}$$

where $J > 0$ or $J < 0$ represents the ferroelastic or antiferro-elastic interaction parameter between the SCO molecules, respectively, and $\Delta_{\mathrm{eff}} = (\Delta - k_B T\ln g)$ is the effective ligand field gap, which includes the quantity, Δ, corresponding to the difference of ligand fields between HS and LS states of isolated molecules and the entropic contribution, $k_B T\ln g$, resulting from the electronic and vibrational degeneracy ratio, $g = \frac{g_{\mathrm{HS}}}{g_{\mathrm{LS}}}$, between the HS and LS states. Using a mean-field treatment of the Hamiltonian (eq 3), which follows very standard developments, we can obtain the following homogeneous free energy:

$$F_{\mathrm{hom}} = \frac{1}{2}Jm^2 - k_BT\ln[2g\cosh(\beta(Jm - \Delta_{\mathrm{eff}}))] \tag{4}$$

where $m = \langle S\rangle$ is the average fictitious magnetization per site and $\beta = \frac{1}{k_BT}$. The minimization of the analytical expression of the free energy, given in eq 4, with respect to the net "magnetization", m, resolving the equation $\frac{\partial F_{\mathrm{hom}}}{\partial m} = 0$ leads straightforwardly to the derived self-consistent eq 5.

$$m = \tanh[\beta(Jm - \Delta_{\mathrm{eff}})] \tag{5}$$

The latter is connected to the HS fraction, n_{HS}, through the relation

$$n_{\mathrm{HS}} = \frac{1 + \langle S\rangle}{2} = \frac{1+m}{2} \tag{6}$$

The resolution of the self-consistent eq 5 gives the temperature dependence of the HS fraction, n_{HS}, which represents the fraction of molecules occupying the HS state stabilized at higher temperatures. Equation 5 admits a solution, $m = 0$, when $\Delta_{\mathrm{eff}} = \Delta - k_BT\ln g = 0$. So, for $m = 0$, corresponding to $n_{\mathrm{HS}} = 1/2$, we derive the transition temperature of the system that cancels the effective field whose expression writes simply as $T_{\mathrm{eq}} = \Delta/(k_B\ln g)$. It is interesting to note that the resolution of eq 5 does not need any numerical simulations to be performed; despite the self-consistent nature of this equation, it can be easily reversed by expressing the temperature as a function of the magnetization

$$T = \frac{2J(1 - 2n_{\mathrm{HS}}) - \Delta H}{k_B\ln\left[\left(\frac{n_{\mathrm{HS}}}{1-n_{\mathrm{HS}}}\right)\right] - \Delta S} \tag{7}$$

Then, changing m from −1 to +1 by accounting for the limits gives, in a unique way, the associated temperature, T.

■ ASSOCIATED CONTENT

Supporting Information

The Supporting Information is available free of charge at https://pubs.acs.org/doi/10.1021/acs.cgd.2c01538.

FT-IR spectra, TGA curves, NMR spectra, and crystal structures of of **1**·3$CHCl_3$ and **1**·2.5CH_2Cl_2 (PDF)

Magnetic behavior of **1**·3$CHCl_3$ (4−300 K) (AVI)

Magnetic behavior of **1**·2.5CH_2Cl_2 (4 to 400 K) (AVI)

Magnetic behavior of **1**·2.5CH_2Cl_2 (400 to 4 K) (AVI)

Accession Codes

CCDC 2232332−2232336 contain the supplementary crystallographic data for this paper. These data can be obtained free of charge via www.ccdc.cam.ac.uk/data_request/cif, or by emailing data_request@ccdc.cam.ac.uk, or by contacting The Cambridge Crystallographic Data Centre, 12 Union Road, Cambridge CB2 1EZ, UK; fax: +44 1223 336033.

■ AUTHOR INFORMATION

Corresponding Author

Yann Garcia − *Institute of Condensed Matter and Nanosciences, Molecular Chemistry, Materials and Catalysis (IMCN/MOST), Université Catholique de Louvain, 1348 Louvain-la-Neuve, Belgium;* orcid.org/0000-0002-3105-0735; Email: yann.garcia@uclouvain.be

Authors

Li Sun − *Institute of Condensed Matter and Nanosciences, Molecular Chemistry, Materials and Catalysis (IMCN/*

https://doi.org/10.1021/acs.cgd.2c01538
Cryst. Growth Des. 2023, 23, 3402−3411

MOST), Université Catholique de Louvain, 1348 Louvain-la-Neuve, Belgium

Nour El Islam Belmouri − *UVSQ, CNRS, GEMAC UMR 8635, Université Paris-Saclay, F78035 Versailles Cedex, France*

Mamadou Ndiaye − *UVSQ, CNRS, GEMAC UMR 8635, Université Paris-Saclay, F78035 Versailles Cedex, France;* orcid.org/0000-0001-9370-379X

Koen Robeyns − *Institute of Condensed Matter and Nanosciences, Molecular Chemistry, Materials and Catalysis (IMCN/MOST), Université Catholique de Louvain, 1348 Louvain-la-Neuve, Belgium;* orcid.org/0000-0002-4763-4217

Aurelian Rotaru − *Department of Electrical Engineering and Computer Science, "Stefan cel Mare" University, Suceava 720229, Romania;* orcid.org/0000-0002-8782-7988

Kamel Boukheddaden − *UVSQ, CNRS, GEMAC UMR 8635, Université Paris-Saclay, F78035 Versailles Cedex, France;* orcid.org/0000-0003-0464-1609

Complete contact information is available at: https://pubs.acs.org/10.1021/acs.cgd.2c01538

Notes

The authors declare no competing financial interest.

■ ACKNOWLEDGMENTS

This work was supported through the Fonds De La Recherche Scientifique (FNRS) (PDR T.0095.21, CDR J.0064.23, and CDR J.0168.22); the Université de Versailles-Paris Saclay, CNRS, and Mol-CoSM ANR project no. ANR-20-CE07-0028-01, the Ministère de l'Education et de la Recherche de Roumanie and WBI. L.S. was supported by a fellowship from the China Scholarship Council (201804910584).

■ REFERENCES

(1) Garcia, Y.; Moscovici, J.; Michalowicz, A.; Ksenofontov, V.; Levchenko, G.; Bravic, G.; Chasseau, D.; Gütlich, P. A Spin Transition Molecular Material with a Wide Bistability Domain. *Chem. Eur. J.* **2002**, *8*, 4992−5000.

(2) Takahashi, K. Spin-Crossover Complexes. *Inorganics* **2018**, *6*, 32.

(3) Garcia, Y.; Gütlich, P. Thermal Spin Crossover in Mn(II), Mn(III), Cr(II) and Co(III) Coordination Compounds. *Top. Curr. Chem.* **2004**, *234*, 49−62.

(4) Gütlich, P.; Gaspar, A. B.; Garcia, Y.; Ksenofontov, V. Pressure effect studies in molecular magnetism. *C. R. Chimie* **2007**, *10*, 21−36.

(5) Jureschi, C. M.; Linares, J.; Rotaru, A.; Ritti, M. H.; Parlier, M.; Dirtu, M. M.; Wolff, M.; Garcia, Y. Pressure sensor via optical detection based on a 1D spin transition coordination polymer. *Sensors (Basel)* **2015**, *15*, 2388−98.

(6) Garcia, Y.; Ksenofontov, V.; Levchenko, G.; Gütlich, P. Pressure effect on a novel spin transition polymeric chain compound. *J. Mater. Chem.* **2000**, *10*, 2274−2276.

(7) Halder, G. J.; Kepert, C. J.; Moubaraki, B.; Murray, K. S.; Cashion, J. D. Guest-dependent spin crossover in a nanoporous molecular framework material. *Science* **2002**, *298*, 1762−1765.

(8) Garcia, Y.; van Koningsbruggen, P. J.; Lapouyade, R.; Fournès, L.; Rabardel, L.; Kahn, O.; Ksenofontov, V.; Levchenko, G.; Gütlich, P. Influences of Temperature, Pressure, and Lattice Solvents on the Spin Transition Regime of the Polymeric Compound [Fe(hyetrz)3]-A2·3H2O (hyetrz = 4-(2′-hydroxyethyl)-1,2,4-triazole and A^- = 3-nitrophenylsulfonate). *Chem. Mater.* **1998**, *10*, 2426−2433.

(9) Breuning, E.; Ruben, M.; Lehn, J.-M.; Renz, F.; Garcia, Y.; Ksenofontov, V.; Gütlich, P.; Wegelius, E.; Rissanen, K. Spin Crossover in a supramolecular Fe_4^{II} [2 × 2] Grid Triggered by Temperature, Pressure, and Light. *Angew. Chem., Int. Ed.* **2000**, *39*, 2504−2507.

(10) Kitazawa, T. Synthesis and applications of new spin crossover compounds. *Crystals* **2019**, *9*, 382.

(11) Lochenie, C.; Bauer, W.; Railliet, A. P.; Schlamp, S.; Garcia, Y.; Weber, B. Large thermal hysteresis for iron(II) spin crossover complexes with *N*-(pyrid-4-yl)isonicotinamide. *Inorg. Chem.* **2014**, *53*, 11563−72.

(12) Gütlich, P.; Gaspar, A. B.; Garcia, Y. Spin state switching in iron coordination compounds. *Beilstein J. Org. Chem.* **2013**, *9*, 342−391.

(13) *Spin crossover in transition metal compounds I*; Gütlich, P., Goodwin, H. A., Eds.; Topics in Current Chemistry, Vol. *1*; Springer Science & Business Media, 2004.

(14) Kitase, K.; Akahoshi, D.; Kitazawa, T. Effects of both Methyl and Pyrimidine groups in Fe-Ag spin-crossover Hofmann-type complex Fe(4-Methylpyrimidine)$_2$[Ag(CN)$_2$]$_2$. *Inorg. Chem.* **2021**, *60*, 4717−4722.

(15) Kitase, K.; Kitazawa, T. A novel two-step Fe-Au type spin-crossover behavior in a Hofmann-type coordination complex Fe(4-methylpyrimidine)$_2$[Au(CN)$_2$]$_2$. *Dalton Trans.* **2020**, *49*, 12210−12214.

(16) Zhu, Q. L.; Xu, Q. Metal-organic framework composites. *Chem. Soc. Rev.* **2014**, *43*, 5468−512.

(17) Cai, G.; Yan, P.; Zhang, L.; Zhou, H. C.; Jiang, H. L. Metal-Organic Framework-Based Hierarchically Porous Materials: Synthesis and Applications. *Chem. Rev.* **2021**, *121*, 12278−12326.

(18) Garcia, Y.; Niel, V.; Muñoz, M. C.; Real, J. A. Spin Crossover in 1D, 2D and 3D Polymeric Fe(II) Networks. *Top. Curr. Chem.* **2004**, *233*, 229−257.

(19) Garcia, Y.; Kahn, O.; Rabardel, L.; Chansou, B.; Salmon, L.; Tuchagues, J. P. Two-Step Spin Conversion for the Three-Dimensional Compound Tris(4,4′-bis-1,2,4-triazole)iron(II) Diperchlorate. *Inorg. Chem.* **1999**, *38*, 4663−4670.

(20) Pineiro-Lopez, L.; Valverde-Munoz, F. J.; Trzop, E.; Munoz, M. C.; Seredyuk, M.; Castells-Gil, J.; da Silva, I.; Marti-Gastaldo, C.; Collet, E.; Real, J. A. Guest induced reversible on-off switching of elastic frustration in a 3D spin crossover coordination polymer with room temperature hysteretic behaviour. *Chem. Sci.* **2021**, *12*, 1317−1326.

(21) Wu, X. R.; Shi, H. Y.; Wei, R. J.; Li, J.; Zheng, L. S.; Tao, J. Coligand and solvent effects on the architectures and spin-crossover properties of (4,4)-connected Iron(II) coordination polymers. *Inorg. Chem.* **2015**, *54*, 3773−80.

(22) Niel, V.; Martinez-Agudo, J. M.; Muñoz, M. C.; Gaspar, A. B.; Real, J. A. Cooperative Spin Crossover Behavior in Cyanide-Bridged Fe(II)-M(II) Bimetallic 3D Hofmann-like Networks (M) Ni, Pd, and Pt). *Inorg. Chem.* **2001**, *40*, 3838−3839.

(23) Galet, A.; Gaspar, A. B.; Muñoz, M. C.; Bukin, G. V.; Levchenko, G.; Real, J. A. Tunable Bistability in a Three-Dimensional Spin-Crossover Sensory- and Memory-Functional Material. *Adv. Mater.* **2005**, *17*, 2949−2953.

(24) Shepherd, H. J.; Bartual-Murgui, C.; Molnár, G.; Real, J. A.; Muñoz, M. C.; Salmon, L.; Bousseksou, A. Thermal and pressure-induced spin crossover in a novel three-dimensional Hoffman-like clathrate complex. *New J. Chem.* **2011**, *35*, 1205.

(25) Bartual-Murgui, C.; Salmon, L.; Akou, A.; Ortega-Villar, N. A.; Shepherd, H. J.; Munoz, M. C.; Molnar, G.; Real, J. A.; Bousseksou, A. Synergetic effect of host-guest chemistry and spin crossover in 3D Hofmann-like metal-organic frameworks [Fe(bpac)M(CN)4] (M = Pt, Pd, Ni). *Chem. Eur. J.* **2012**, *18*, 507−16.

(26) Pineiro-Lopez, L. A.; Valverde-Munoz, F. J.; Seredyuk, M.; Munoz, M. C.; Haukka, M.; Real, J. A. Guest induced strong cooperative one- and two-step spintransitions in highly porous Iron(II) hofmann-type metal-organic frameworks. *Inorg. Chem.* **2017**, *56*, 7038−7047.

(27) Rubio-Giménez, V.; Escorcia-Ariza, G.; Bartual-Murgui, C.; Sternemann, C.; Galbiati, M.; Castells-Gil, J.; Real, J. A.; Tatay, S.; Martí-Gastaldo, C. Ultrathin Films of 2D Hofmann-Type Coordina-

tion Polymers: Influence of Pillaring Linkers on Structural Flexibility and Vertical Charge Transport. *Chem. Mater.* **2019**, *31*, 7277−7287.
(28) Valverde-Munoz, F. J.; Bartual-Murgui, C.; Pineiro-Lopez, L.; Munoz, M. C.; Real, J. A. Influence of host-guest and host-host Interactions on the spin-crossover 3D Hofmann-type clathrates {Fe(II)(pina)[M(I)$(CN)_2$]$_2$}.xMeOH (M(I) = Ag, Au). *Inorg. Chem.* **2019**, *58*, 10038−10046.
(29) Bartual-Murgui, C.; Rubio-Gimenez, V.; Meneses-Sanchez, M.; Valverde-Munoz, F. J.; Tatay, S.; Marti-Gastaldo, C.; Munoz, M. C.; Real, J. A. Epitaxial Thin-Film vs Single Crystal Growth of 2D Hofmann-Type Iron(II) Materials: A Comparative Assessment of their Bi-Stable Spin Crossover Properties. *ACS Appl Mater Interfaces* **2020**, *12*, 29461−29472.
(30) Meneses-Sánchez, M.; Piñeiro-López, L.; Delgado, T.; Bartual-Murgui, C.; Muñoz, M. C.; Chakraborty, P.; Real, J. A. Extrinsic vs. intrinsic luminescence and their interplay with spin crossover in 3D Hofmann-type coordination polymers. *J. Mater. Chem. C* **2020**, *8*, 1623−1633.
(31) Turo-Cortes, R.; Bartual-Murgui, C.; Castells-Gil, J.; Munoz, M. C.; Marti-Gastaldo, C.; Real, J. A. Reversible guest-induced gate-opening with multiplex spin crossover responses in two-dimensional Hofmann clathrates. *Chem. Sci.* **2020**, *11*, 11224−11234.
(32) Ni, Z.-P.; Liu, J.-L.; Hoque, M. N.; Liu, W.; Li, J.-Y.; Chen, Y.-C.; Tong, M.-L. Recent advances in guest effects on spin-crossover behavior in Hofmann-type metal-organic frameworks. *Coord. Chem. Rev.* **2017**, *335*, 28−43.
(33) Agustí, G.; Cobo, S.; Gaspar, A. B.; Molnár, G. b.; Moussa, N. O.; Szilágyi, P. Á.; Pálfi, V.; Vieu, C.; Muñoz, M. C.; Real, J. A.; Bousseksou, A. Thermal and Light-Induced Spin Crossover Phenomena in New 3D Hofmann-Like Microporous Metalorganic Frameworks Produced As Bulk Materials and Nanopatterned Thin Films. *Chem. Mater.* **2008**, *20*, 6721−6732.
(34) Sun, L.; Ndiaye, M.; El Islam Belmouri, N.; Robeyns, K.; Rotaru, A.; Boukheddaden, K.; Garcia, Y. Spin crossover coordination polymers with pyridine-Like modification through selective guest Molecules. *Cryst. Growth Des.* **2022**, *22*, 7555−7563.
(35) Garcia, Y.; Campbell, S. J.; Lord, J. S.; Linares, J.; Dîrtu, M. M.; Vendrell Pérez, A.; Boland, Y.; Ksenofontov, V.; Gütlich, P. Spin conversion detected by Mössbauer spectroscopy and μSR on a 1D Fe^{II} paramagnetic chain. *Hyperfine Interact.* **2014**, *226*, 217−221.
(36) Fourati, H.; Boukheddaden, K. Experimental evidence for the elastic long-range character of the spin crossover transition in cooperative single crystals. *Phys. Rev. B* **2020**, *101*, 224101.
(37) Varret, F.; Chong, C.; Slimani, A.; Garrot, D.; Garcia, Y.; Naik, A. D. Real-time observation of spin-transitions by optical microscopy. In *Spin-Crossover Materials: Properties and Applications*; Halcrow, M. A., Ed.; Wiley-VCH, 2013; pp 425−441.
(38) Chong, C.; Mishra, H.; Boukheddaden, K.; Denise, S.; Bouchez, G.; Collet, E.; Ameline, J.-C.; Naik, A. D.; Garcia, Y.; Varret, F. Electronic and structural aspects of spin transitions observed by optical microscopy. The case of [Fe $(ptz)_6$]$(BF_4)_2$. *J. Phys. Chem. B* **2010**, *114*, 1975−1984.
(39) Fourati, H.; Ndiaye, M.; Sy, M.; Triki, S.; Chastanet, G.; Pillet, S.; Boukheddaden, K. Light-induced thermal hysteresis and high-spin low-spin domain formation evidenced by optical microscopy in a spin-crossover single crystal. *Phys. Rev. B* **2022**, *105*, 174436.
(40) Boukheddaden, K.; Fourati, H.; Singh, Y.; Chastanet, G. Evidence of photo-thermal effects on the first-order thermo-induced spin transition of [{Fe(NCSe)$(py)_2$}$_2$(m-bpypz)] spin-crossover material. *Magnetochemistry* **2019**, *5*, 21.

https://doi.org/10.1021/acs.cgd.2c01538
Cryst. Growth Des. 2023, 23, 3402−3411